Chapter 3

Recognition based on segmentation

This chapter adresses the problem of structural texture recognition based on the segmentation of its primitives or *textons*. In many cases, textures can be classified taking the images as a whole, that is, computing image features such as the classical co-ocurrence matrices. However, structural textures (those exhibiting a more or less regular pattern of primitives) can be analyzed by computing descriptive measures of their individual primitive elements, like shape features, spatial, size and grey level or colour distributions.

This is the approach taken here, and it is illustrated with a practical problem, namely the recognition of marble samples from ornamental stones and statues of the Roman period. It is a first approach to the classification problem for those textured images based on a structural point of view. We want to classify a marble sample in a similar way as the expert works but using image processing techniques. Microscopy marble images are textured images where grains correspond to the structural elements (see Fig. 3.2). These grains observed globally as a structural texture permit to identify the provenance quarry of a marble sample. Experts can distinguish among several quarries by the size, shape and relations among the grains of a marble sample viewed through a petrographical microscope.

To study the shape of the grains, firstly we need to partition the image in those grains. This preliminary grain segmentation used later by an expert for classification purposes is the main contribution of this chapter. Later, a classification of a sample in one of those quarries can be done studying the morphology of grains and the topological relation among them. But, being the classification fully application-dependend (and unrelated to the wavelet transform), we consider it a secondary issue.

Wavelets, the connecting theme of the whole dissertation, are introduced as an auxiliary tool in this process and is not related directly to the classification process as in next chapter, but it was our first contact to this vast field. Here, wavelets are introduced as a filtering step necessary to prevent an excessive oversegmentation. They improve previous results obtained with mathematical morphology techniques. These two filtering strategies, mathematical morphology and wavelet transform, are compared in our previous works [60, 61]. Therefore, the main focus is on segmentation of textons and their statistical classification based on simple mesures on them.

3.1 Introduction

The method we present is part of a more general project about the determination of geographical origin of ornamental stones used in the Roman period. The final goal is to classify a marble sample into one of several quarries to contribute to the knowledge of the trading routes from that period. Provenance identification is important in discovering exchanges between populations, dating artifacts, and identifying forgeries and copies.

Marble recognition has been performed by means of techniques based on physical, chemical and visual properties of samples [40], such as the analysis of different element traces, stable isotopes, X-ray spectroscopy and diffraction, distribution and size of pores, etc. Methods based on visual features are liable to be automated by digital image analysis [56, 3]. This usually represents a higher speed of classification and greater flexibility of the implementation at a relatively low cost.

The visual recognition of marble samples is carried out studying thin marble sections viewed through a petrographical microscope. It takes into account the shape, size and spatial distribution of grains, factors related to the marble petrogenesis. In Fig. 3.2 we can see ten samples of microscopic images of marble used in this work. Visually, it is easy to dicern some classes; for example, Carrara samples are recognized by the regular shape and uniform size of their little grains, whereas Paros samples show two dominant different sizes, Almadén has macles in abundance, and the contours of grains in Naxos are irregular, etc. All these features related to the visual properties of grains are used for skilled professionals to classify samples.

We have studied samples of ten quarries; Section 3.2 describes these samples and how they were acquired by our system composed of a microscope and a camera. We take profit of the optical properties of this kind of material observed throught the micorscope to refine the segmentation results. Each grain in a thin marble section has its own preferred direction, usually different from those of neighbouring grains. Therefore, when we change the angle between the analyzer and polarizer in a petrographical microscope, each grain exhibits a different and characteristic pattern of intensity variation of incident light transmission. This is due to the response of these materials to polarized light, and this is explained in Section 3.3. An expert uses those properties in order to distinguish the grains, and so does our method.

An overview of the segmentation process is represented in Fig. 3.1, which summarizes the flow of data and the important steps from the acquisition to the final segmentation. First of all, we capture an image without polarizer, besides we take two sequences of images, each sequence corresponding to a fixed polarizer position. Thus, by varying the analyzer angle, we obtain the images for each sequence. Next, we perform photometric and geometric corrections to images in order to process later all these images (Section 3.4). At this point, we also calculate two parameters that are related to the preferred direction at each point. They are the amplitude and phase of the sinusoidal intensity pattern that exhibits each point within a grain and are computed from the two sequences of polarization images (Section 3.4.4). To start the segmentation process, we perform a filtering step to reduce the number of regions obtained (Section 3.6). We propose two solutions to this step. The first one is based on mathematical morphological transformations, and was inspired by the fact

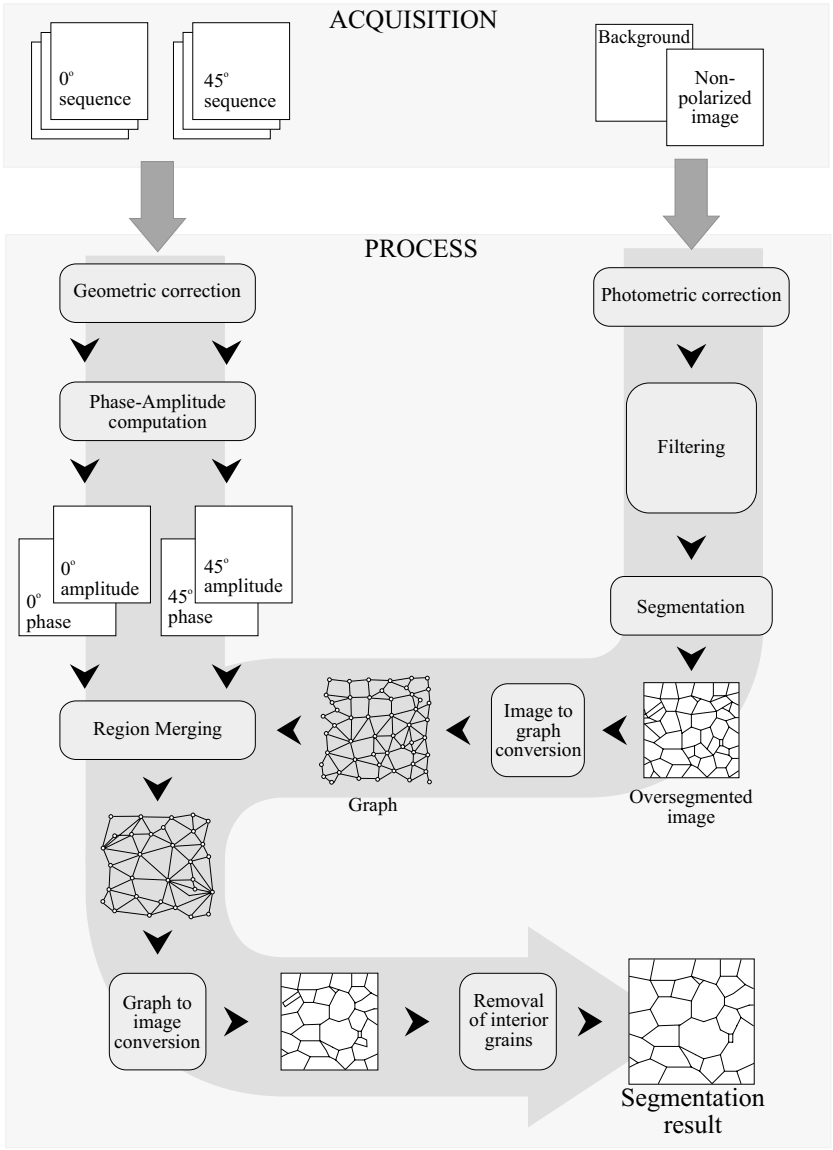

Figure 3.1: Scheme of the segmentation method.

that the final segmentation is performed by a watershed transformation which is a mathematical morphological transformation. Later, we studied the field of wavelets and tried to adapt some of these techniques to our problems, and so we began by solving this filtering step. Using this approach, we get better results than simply adapting traditional non-linear filtering schemes in the literature based on wavelets. Our method does a wavelet decomposition of the non-polarized image and reconstruct

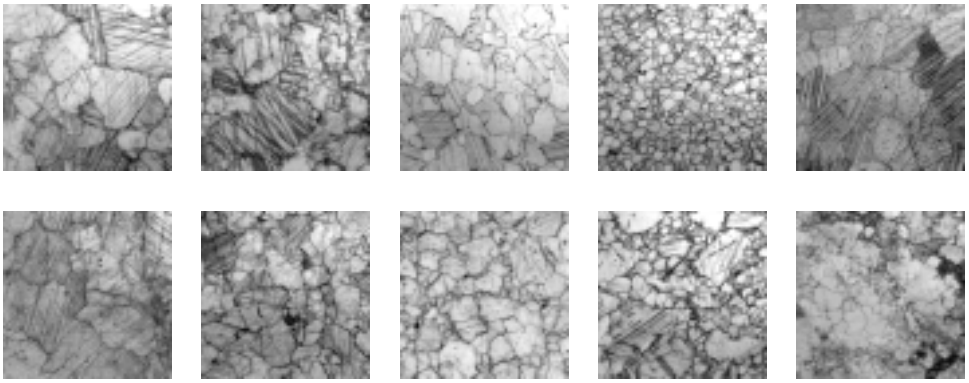

Figure 3.2: Samples of petrographical microscopic images of marbles of different quarries. From top to bottom and from left to right: Aphrodisias, Almadén, Afyon, Carrara, Estremoz, Naxos, Paros, Pentelikon, Proconneso, Saint-Béat.

it but just with a subset of the detail coefficients. Thus, with any of the two methods, we achieve a smooth image suitable to be oversegmented by means of a watershed transform (Section 3.5). Next, in Section 3.7, regions belonging to the same grain are merged according to a similarity measure depending on the amplitude and phase; grains located inside other grains have been removed from the merged image. In Section 3.8, we show and discuss the results obtained in the segmentation. In Section 3.9, we point out some properties useful for the classification of samples, and finally we finish with some conclusions in Section 3.11.

Figure 3.1 shows graphically the global process previous to the classification. The left column of the process with the amplitude and phase calculation is mainly devoted to refine results obtained in the segmentation step. The right part works with a simple image, and can be extended easily to other similar segmentation problems not restricted to the microscopic field as we explain in Section 3.10.

3.2 Material

We have studied samples of marbles coming from the following quarries: Carrara (from Italy); Paros, Pentelikon, Naxos (from Greece); Proconnesos, Aphrodisias, Afyon (from Turkey); Almadén (from Spain); Saint-Béat (from France) and Estremoz (from Portugal). Figure 3.2 shows one sample image of each one of these quarries. They have been sliced up from pieces of sculptures or building elements belonging to the Greek and Roman periods. We find in them a broad range of grain shapes and sizes, although all of them are made of calcite, an uniaxial crystal[1].

Samples are 3 cm long, 2 cm wide and 30 to 40 μm thick. To examine them, we have used a petrographical microscope Leitz Ortolux. Its analyzer has a precision of

[1] anisotropic media where refraction index varies according to the vibration direction of the light into the crystal [10].

0.1 degrees, and the polarizer can be put into two positions, 0 and 90 degrees. We have chosen for each sample the objective lens that, keeping a reasonable grain size, visualized a sufficient number of grains for classification purposes. Digital images were directly captured from the petrographical microscope with a black and white CCD camera connected to an acquisition Matrox board. Images resolution is 512×512 pixels and 256 grey levels.

Our method has been implemented as a set of independent functions, each one devoted to a specific task: correction, segmentation, classification. These functions are not stand-alone because they are integrated in ViLi, an image processing and analysis environment conceived by the Computer Vision Center of the Universitat Autònoma de Barcelona. ViLi image processing functions are programmed in C or Lisp. Both kind of functions can be then called from the Lisp interpreter. Complex functions, usually involving pixel-level operations, are programmed in C. Thus, we take advantage of the speed and the control and data structures which this language offers. On top of them, we write Lisp functions that play the role of main programs, but are much easier to build and debug than C programs. ViLi includes more than two hundred C and Lisp image processing functions, which can be invoked from any Lisp or C ViLi program. This flexibility permits to build complex software environments based on ViLi [81] with a fast transition from test coding to final program.

3.3 Petrographical model of marble images

The amount of intensity that passes through an uniaxial crystal placed between two nicols, as Fig. 3.3 shows, is given by the Johannsen's equation Eq. (3.1) [102]. It relates the incident intensity of light $I_i(\lambda)$ that illuminates a sample to the intensity transmitted (observed) through a petrographical microscope $I_o(\lambda)$:

$$I_o(\lambda) = I_i(\lambda) \left(\cos^2(\phi) - \sin(2\tau)\, \sin(2(\tau - \phi))\, \sin^2\left(\pi \frac{\Delta}{\lambda}\right) \right) \quad , \tag{3.1}$$

being

- λ the light wavelength.
- Δ the difference in trajectory between the fast and slow waves as the light goes through the crystal.
- ϕ the angle between the analyzer and polarizer preferred directions.
- τ the angle between the polarizer and the crystal preferred directions.

Therefore, τ and Δ are characteristics of each grain. If the light source emits in a spectral range Λ then the relation between the incident and transmitted intensities, I_i and I_o respectively, is

$$I_o = I_i \cos^2(\phi) - \sin(2\tau)\, \sin(2\tau - 2\phi) \int_\Lambda I_i(\lambda)\, \sin^2\left(\pi \frac{\Delta}{\lambda}\right) d\lambda \quad . \tag{3.2}$$

Δ is constant inside each grain. Thus, Eq. (3.2) can be simplified by defining

$$\int_\Lambda I_i(\lambda)\, \sin^2\left(\pi \frac{\Delta}{\lambda}\right) d\lambda = K I_i \quad ,$$

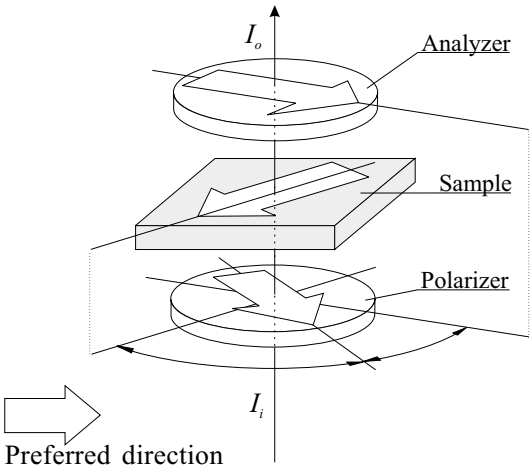

Figure 3.3: Preferred directions in a petrographical microscope.

where $0 \leq K \leq 1$. Note at this point that the value of K and τ are unknown at each grain. However, our goal is not to calculate them but to investigate how they affect the transmitted intensity depending on the angle ϕ between the analyzer and the polarizer, which we can control. Let us rewrite Eq. (3.2) by grouping the terms depending on ϕ:

$$I_o = I_i \left(\cos^2(\phi) - K \sin(2\tau)\, \sin(2\tau - 2\phi)\right) = \frac{I_i}{2}\left(1 + A\cos(2\phi) + B\sin(2\phi)\right) \ ,$$

where $A = 1 - 2K\sin^2(2\tau)$ and $B = K\sin(4\tau)$. This expression gets simpler if we define two new variables $C = \sqrt{A^2 + B^2}$ and $D = \arctan(B/A)$ that are the radius and the angle of (A, B) expressed in polar form:

$$I_o = \frac{I_i}{2}(1 + C\cos(2\phi - D)) \ . \tag{3.3}$$

Hence, I_o is a sinusoidal function of amplitude $M = C\,\dfrac{I_i}{2}$ and phase D, both values being function of K and τ which are characteristic of each grain. Thus, the computation of M and D for each pixel will greatly help us to differentiate adjacent grains.

However, there is still one problem concerning the computation of D. If we fix the polarizer position, we observe that the transmitted intensity at some grains is quite low and does not change significantly when we modify the analyzer angle (Fig. 3.4). The reason is that in those grains the amplitude M is very small. Therefore, the phase D computed from the intensities $I_o(\phi)$ will not be reliable because of the low signal-to-noise ratio (see Section 3.4.4). In order to overcome this problem we acquire a second sequence of images but at a different polarizer angle. Let us see which one is the most suitable.

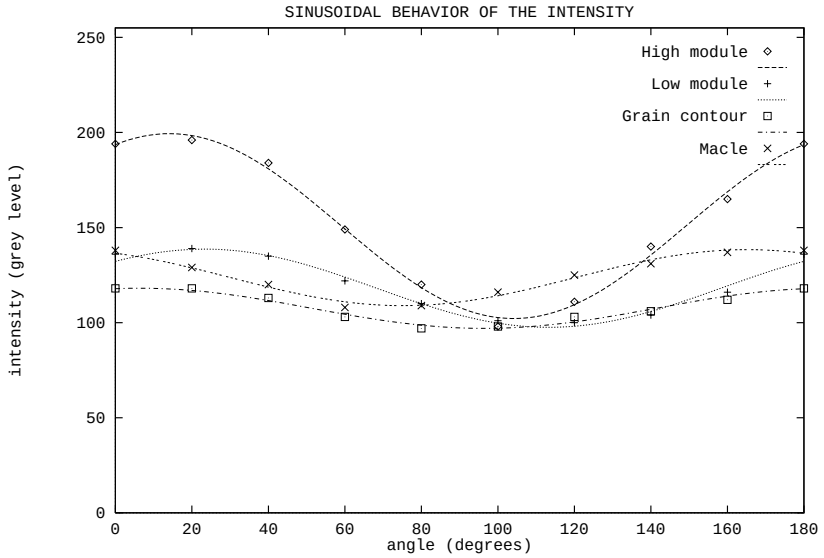

Figure 3.4: Intensity behaviour at different points in a sequence where the polarizer angle varies. We have also represented function $M\cos(2\phi - D)$, with M and D estimated from $F(1)$, the first harmonic.

M is a function of K and τ. As we can not change K, we shall look for the value of τ which maximizes M:

$$\frac{d(M^2)}{d\tau} = K(K-1)\sin(4\tau) = 0 \ .$$

Extrema are found at $\tau = \frac{\pi}{4}k$ and maxima at $\tau = \frac{\pi}{2}k$, $k \in \mathbb{N}$. Thus, by taking two sequences of images with their polarizer angle 45 degrees apart, i.e. $0°$ and $45°$, we guarantee a high amplitude and a reliable phase for each grain, at least in one of the two sequences. Finally, although there are a good agreement between the sinusoidal behaviour predicted in Eq. (3.3) and the data, as we see in Fig. 3.4, there is a slight difference on the constant term but unimportant in the phase and amplitude computation.

3.4 Image samples and preprocessing stage

3.4.1 Acquisition

According to the former image formation model explained in Section 3.3, for each zone of a marble sample that we want to segment, we capture the following images:

- An image without analyzer nor polarizer, I_s .
- A background image, taken without any sample, I_b .

- A sequence of N images $\{I_0(\phi_k)\}, k = 0 \ldots N-1$ with the polarizer at $0°$ and the analyzer at different, equally spaced positions ϕ_k .
- A second sequence $\{I_{45}(\phi_k)\}, k = 0 \ldots N-1$ with the polarizer at $45°$ and the same positions for the analyzer as the previous case.

The two first images are used to obtain a preliminary segmentation and the two other sets try to refine this segmentation. Figure 3.1 shows all these images at the top of the scheme as inputs to the global process.

3.4.2 Photometric correction

Lighting of I_s is not homogeneous, as can be seen in the background image I_b of Fig. 3.6b. Microscope optics can also introduce some lesser photometric distortions. We must correct I_s to make sure that the transformations we shall apply on it will be spatially invariant, that is, they will have the same effect everywhere. The non-polarized and background images can be modeled as transparent matters with a response to the light ruled by some transmittance factors (see Fig. 3.5).

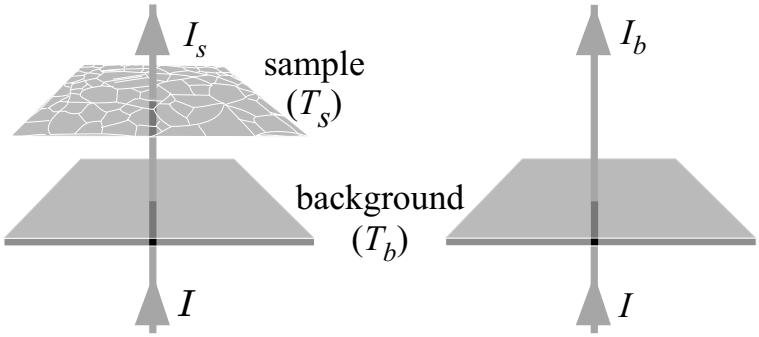

Figure 3.5: Intensity formation model based on the transmitance of the samples.

Therefore, intensities images represent:

$$\begin{aligned} I_s &= I\,T_b\,T_s \\ I_b &= I\,T_b\ , \end{aligned} \tag{3.4}$$

where I represents an ideal, completely homogeneous incident lighting, T_s is the sample transmittance and T_b the background and microscope optics transmittance, to which we transfer all the inhomogeneity defects of the real lighting [16]. The image we are interested in is just the sample transmittance $T_s = I_s/I_b$. In practice, in order to accelerate computations, we shall work with a 256 levels (one byte/pixel) quantization of T_s (Fig. 3.6c) instead of its floating point version.

3.4.3 Geometric correction

A second problem we have come across is that images from the sequences exhibit a slight displacement (up to 6 pixels) according to the non-polarized image. This is

(a) (b) (c)

Figure 3.6: Illumination correction: (a) I_s, (b) I_b, (c) $T_s = I_s/I_b$.

possibly due to a deviation of light caused by the analyzer of the microscope. For each image from a sequence we must find out its displacement and then translate the image according to the opposite vector. The alignment of images is essential because the amplitude and phase at each point are computed from the intensities at the same coordinates along the sequences.

To compute the displacement vector we use the correlation [32] that is given by:

$$f(r,s) \circ g(r,s) = \sum_{i=-N}^{N} \sum_{j=-N}^{N} f(i,j)\, g(r+i, s+j) \ \ ,$$

which is a similarity measure in the sense of linear dependency, in particular identity. Equations (3.3) and (3.4) show that there is not a linear relationship between the non-polarized image and an image of any sequence. Despite of it, the intensity in the border of grains does approximately coincide in both images. Therefore, we compute the correlation of their gradient magnitude, approximated as the absolute difference between the local maximum and minimum in a 3×3 window:

$$\| \bigtriangledown f \| \, (r,s) \approx | \max f(r+i, j+s) - \min f(r+i, j+s) |, \quad -1 \leq i,j \leq 1 \ \ .$$

The displacement vector goes from the center of the correlation image to its maximum. The right part of Fig. 3.7 shows different types of correlation results and all they have this maximum peak. We choose the pixel with the maximum value and do not compute a better approximation (subpixel level) because the later calculations do not require so much accuracy.

We also prove a phase correlation to calculate the displacement vector. In this case we have a peak that is sharper than previous (Fig. 3.7f). The vector also comes from the center of the image to the maximum peak. This phase correlation is based in the fact that in the spectral domain most part of the important information of a signal is coded in the phase and not in the magnitude (see [41] for a brief introduction). To calculate this phase correlation we should remove the amplitude of the two signals to be compared. Also, we use the correlation property that link correlation in the

spacial domain with the product in the frequential domain:

$$\mathrm{corr}(f,g) = f(x,y) \circ g(x,y) \Longleftrightarrow F(u,v)\,G^*(u,v) \ ,$$

where $*$ represents the complex conjugate and a capital letter for a function means its Fourier Transform. Therefore, the phase correlation formula is given by

$$\mathrm{corr}_{ph}(f,g) \Longleftrightarrow \frac{F(u,v)\,G^*(u,v)}{|F(u,v)\,G^*(u,v)|} \ .$$

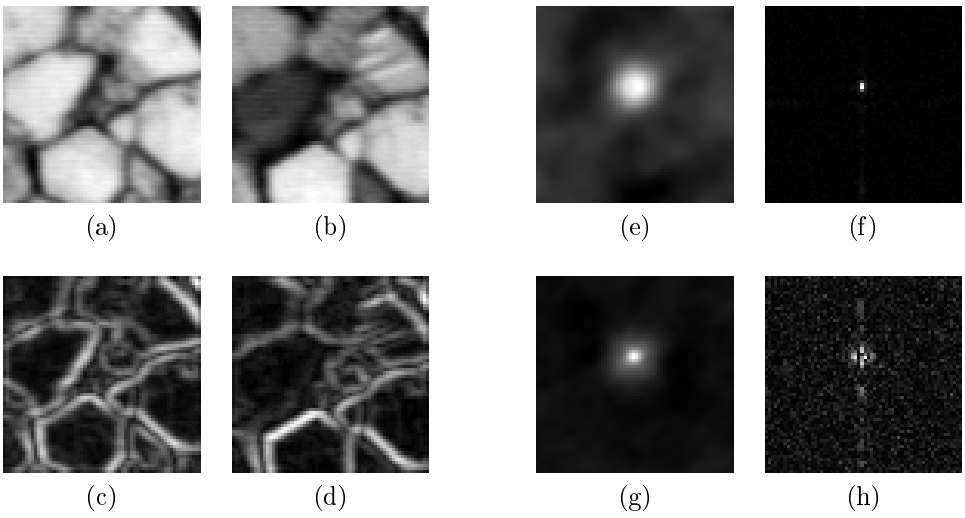

Figure 3.7: Geometric correction based on correlation: (a) I_m, the image without polarizers; (b) $I_0(0^\circ)$, one of the images of the sequences to be corrected; (c) gradient of (a); (d) gradient of (b); (e) correlation of (a) and (b); (f) phase correlation of (a) and (b); (g) correlation of (c) and (d); (h) phase correlation of (c) and (d).

The reason to decide computing this displacement based on the correlation of the gradients in front other solutions is due to the stability of the solutions. Phase correlation gives better accuracy but is most sensitive to the noise and differences between the two image to compare. The solution adopted in this point is showed in Fig. 3.7g as the correlation of the gradients of the two images. It is an intermediate solution between phase correlation of the image (sharp and unstable Fig. 3.7f) and correlation of the two images (smooth and stable Fig. 3.7e). The case showed in Fig. 3.7h is only illustrative of a very unstable solution that has not been evaluated, there are also localization but the noise is amplified.

3.4.4 Phase and amplitude computation

As we see in Section 3.4.1, for each zone of a marble sample to be segmented, we capture two sequences of images with different polarizer orientation. For each sequence

$\{I_0(\phi_k)\}, \{I_{45}(\phi_k)\}, k = 0 \ldots N-1$ we compute phase D and amplitude M at each point by means of the Discrete Fourier Transform (DFT).

If f is a sinusoidal function of period N, it can be seen that the first harmonic $F(1)$ conveys all the important information and $F(u) = 0$ for $u = 2 \ldots N-1$. Due to noise, in addition to sampling and quantization errors, the intensity at each pixel along the sequences is not a pure sinusoidal function. The second and following harmonics are not zero although they are so small in magnitude that can be discarded. Summarizing, in order to obtain the phase and amplitude of a sequence I_p, $p = 0, 45$ at a point (i, j), we only need to compute the first harmonic of $\{I_p(\phi_0, i, j), I_p(\phi_1, i, j), \ldots I_p(\phi_{N-1}, i, j)\}$.

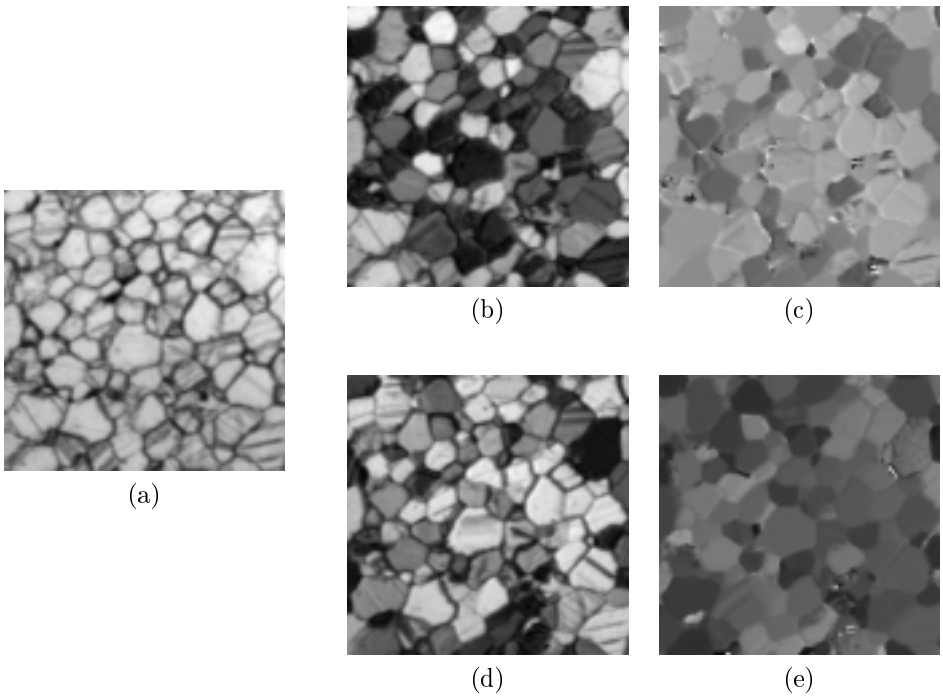

Figure 3.8: Phase and amplitude images: (a) detail of a Carrara sample, (b) amplitude at 0°, (c) phase at 0°, (d) amplitude at 45°, (e) phase at 45°.

$F(1)$ is computed from a sequence of intensity values within one period. If we decide to take sequences of N images then $\phi_k = k\pi/N, k = 0 \ldots N-1$, because I_o has frequency 2ϕ. The larger the number of images N, the more precise the computation of $F(1)$. However, our experience shows that segmentation results are satisfactory for the most of marble samples just with three images per sequence, captured with $\phi_1 = 0°$, $\phi_2 = 60°$ and $\phi_3 = 120°$. Three samples are also the minimum number of samples necessary to perform this computation. Reducing the number of these images we obtain also a reduction of the acquisition time and therefore an increase of the response time of the system. Figure 3.8 shows the images of amplitude and phase

at 0° and 45° for a Carrara sample. An important thing at this point is that macles have been removed in the phase images an this fact is used later in Section 3.7 to join wrongly segmented grains.

3.5 Segmentation

The purpose of the segmentation step is to partition the image I_s into regions, each one belonging to only one grain, although grains can be split into several, but not too many regions (oversegmentation). Thus, we shall just have to merge regions suitably in order to obtain the final segmentation. The oversegmentation step is based on the watershed transform [101, 66, 8] coming from the mathematical morphology field [85]. It divides the image into influence regions of local minima. Let us suppose that it is raining on our topographical relief. When a drop of water falls on the surface, it follows the steepest descent path until it reaches a local minimum. The region of influence of that local minimum is the set of such points and their paths, that is, its slope basin. The watershed transform computes all those slope basins or, equivalently, the divide lines. Watershed algorithms are quite complex, and their description is outside the scope of this work. References [85, 101] describe two different implementations of watersheds.

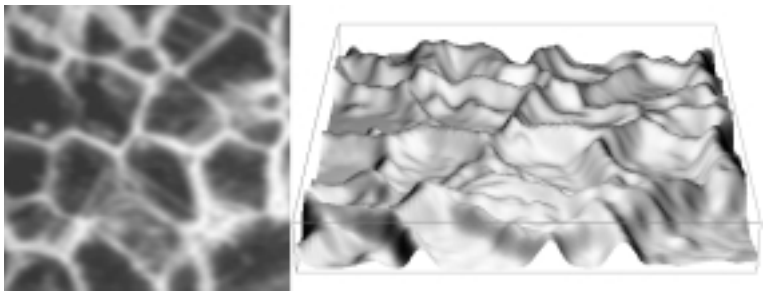

Figure 3.9: Inverted image t_m and its topographical relief.

If we invert the I_s image, and plot it taking grey level as height (Fig. 3.9), we realize that grains appear as slope basins separated by narrow crests, which are macles (junctions between twin crystals) or the boundaries of grains. However, if the watershed transform is directly applied to the inverted image $-I_s$, an excessive oversegmentation is obtained. The reason is the large number of intensity variations that, despite of being small, give rise to too many local minima. These variations are due to several contributions: non-uniform illumination, imperfect grains, and acquisition noise.

To establish watershed as the best method to segment these images we isolate the problem and try to compare different possibilities to reach the expected result. Note that sometimes we talk about watershed and sometimes about watercourses. The two are related because watercourse is the dual operation of watershed: results obtained from watershed in an image are those obtained from watercourses in the inverted image. If we think on the grains image as a topological relief (see Fig. 3.9), the segmentation of grains where the boundaries of each grain must be detected, turns

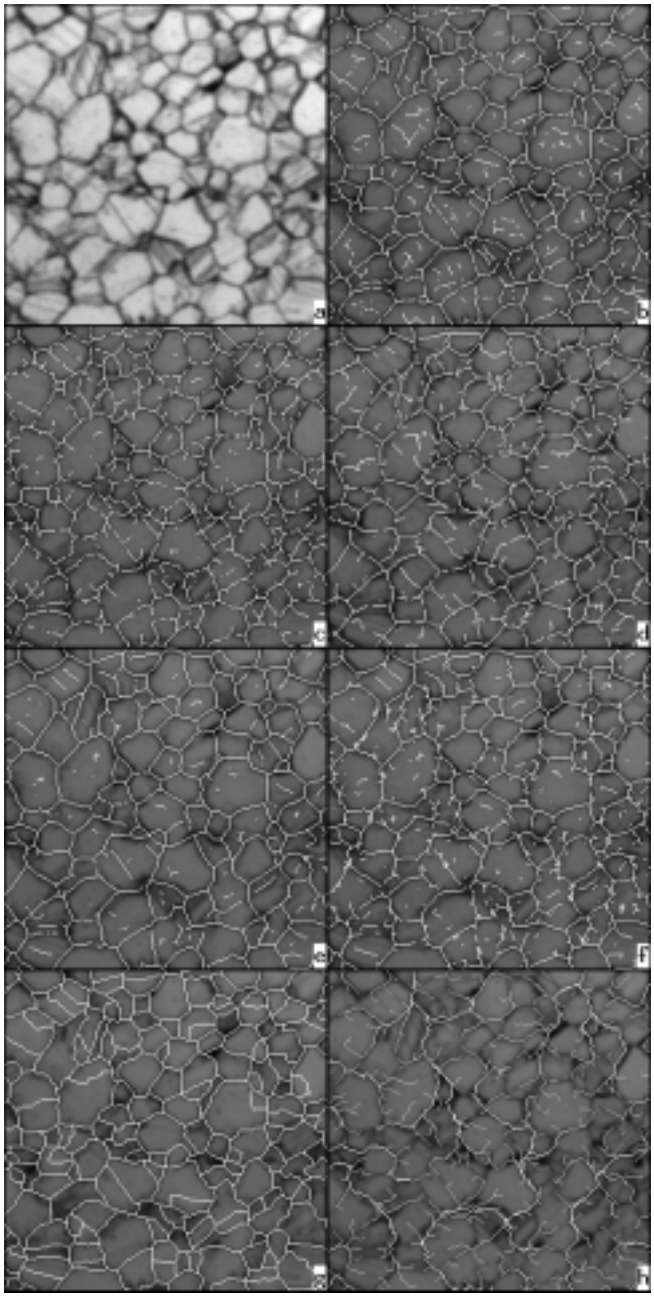

Figure 3.10: (a) Petrographical microscope image of a thin marble section. Valleys based on: (b) negative large values of κ; (c) positive large values of Lvv; (d) vertex condition for valleys; (e) negative large values of $\mathsf{C}\tilde{\kappa}^{\circ}$; (f) height condition for valleys; (g) watercourses; (h) drainage patterns. See [53] for an in-depth description of all these operators.

to a ridge detection problem. Trying to segment this image is similar to calculating these valleys. The same could be formulated for the inverted image changing valleys for ridges.

Globally, specific algorithms for ridges/valleys could be categorized in: extraction of medial axis, medialness approximation, segmentation, and extraction of drainage patterns [55]. Each one of these applications must fulfill their specific properties like: no over-detection, no under-detection, continuity, good contrast, structural stability, and good localization. Specifically, one of the important properties for segmentation applications and therefore in our problem, consist on to get closed regions. Each grain must be associated to one or more of these closed regions; there are not 'open' grains in the real world.

Comparison of different procedures to obtain the ridges and valleys of an image [55] shows how watershed/watercourse transform is, in general, the best ridge/valley method for segmentation purposes. Usually, a suitable filtering scheme to remove local minima or a reliable set of markers is mandatory. We implement the filtering scheme because markers need to be placed for an external user by hand or presuppose the knowledge of the position of something related to each grain. Two strategies for the filtering scheme have been designed and fitted to this problem and they are exposed in Section 3.6. An application-dependent region merging postprocessing is also a good solution also needed in our problem, in which the optical properties of these samples are used to refine results. Figure 3.10 shows a segmentation of marble grains for comparison purposes performed with the techniques explained in our previous cited work. The drainage patterns (Fig. 3.10h) do not follow the grain boundaries as drainage lines of equal relevance. They suffer of bad localization. Crease operators give acceptable results (Figs. 3.10b, c, d, e, f), an implementation of these algorithms can be found in [53, 54]. However, none of these operators ensure closed regions, unlike the case of watercourses (Fig. 3.10g). The response of the multilocal creaseness measure (Fig. 3.10e) explained in [53] could be postprocessed to give such closed regions too. However, despite having fewer regions that with watercourses (compare Figs. 3.10e and 3.10g), we still could not ensure that each one corresponds to a different grain. Therefore, anyway we had to build an application-dependent region grouping procedure. Thus, the watershed algorithm is judged to be the most suitable.

3.6 Filtering process

This is an step that must be done before segmentation. It is explained later because as we conclude in the previous section we choose watershed transformation as the best solution to our problem, but all these ridge/valleys detection techniques need a pre-processing or post-processing stage to achieve good results. We also concluded that in the specific case of watershed it is mandatory a previous filtering step to reduce the oversegmentation produced by noise (see Fig. 3.11a). Next, we explain the two methods that we propose to solve this part. They has been used and adjusted to this specific problem but they can be extended to other problems as we show later.

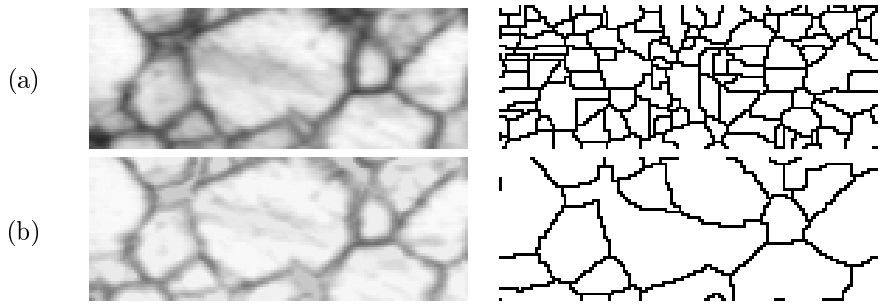

Figure 3.11: Oversegmentation and segmentation: (a) initial image and watershed of its inverse, (b) smoothing by erosion-reconstruction and watershed of its inverse.

3.6.1 Erosion-reconstruction approach

To overcome the oversegmentation problem due to noise, we previously smooth the image by means of an erosion-reconstruction filter [85]. This morphological filter consists of a local minimum transform followed by a series of local maximum transforms conditioned to the original image. The local neighborhood considered is a square of 5×5 dimension, but results are stable for a little variation of this parameter [56]. Figure 3.11 compares the watershed of an inverted transmittance image with and without previous smoothing.

The erosion step applied to the inverted image tries to remove the noise of the image preserving grain edges. The following reconstruction step fills up the grains to their original volume without reviving the noise. Figure 3.12 shows the two steps of this filtering scheme.

Later, some authors [86] have used a similar scheme based on erosion-reconstruction and watershed in segmentation problems of textured colour images achieving also good results. We try to extend the segmentation process to different images from the marble case with also good results, this can be see as a further extension in Sec. 3.10.

3.6.2 New wavelet filtering approach

In this second case we perform the filtering stage, previous to the watershed, with a tool not in the field of the mathematical morphology. Results obtained with linear transformations based on the convolution with a kernel do not improve results obtained with the erosion-reconstruction approach. We started to study wavelet transforms and saw them as a possible solution.

The wavelet transform is better adapted than Fourier analysis to non-periodic signals. Images, unlike other kind of signals have this non-periodic behavior, therefore linear schemes that presuppose periodicity do not fulfil this basic requirements. Nonlinear filtering based on wavelet decomposition as Donoho [25] proposes achieve the removal of noise in images without distort edges. In our case, applying this kind of algorithm directly to marble images does not give the expected results because the next transform applied to the images, watershed, needs the reinforcement of the